PAPER

Check for updates

Interfacial nanobubbles' growth at the initial stage of electrocatalytic hydrogen evolution†

Jinwen Yu,‡[a] Kadi Hu,‡[b] Zhengyi Zhang,[a] Liang Luo, [iD] *[a] Yiwei Liu,[a] Daojin Zhou,[a] Fengmei Wang, [iD] [a] Yun Kuang,[a] Haijun Xu, [iD] [a] Hui Li, [iD] *[b] Haohong Duan [iD] [c] and Xiaoming Sun [iD] *[a]

Bubble evolution in electrolysis, commonly originating from nanobubbles (NBs), usually gives rise to the extra overpotential due to a high internal pressure generated in these ultrasmall sized bubbles. The study on the growth of interfacial NBs is crucial, but nanobubble evolution during electrolysis is still vague. Herein, we employ the *in situ* electrochemical surface plasmon resonance imaging method, combined with atomic force microscopy measurement, to visualize the formation and growth of interfacial NBs during the initial stage of the hydrogen evolution reaction. We find that NB growth originates from pancake shaped ones, followed by increasing the coverage and roughly pinned three-phase boundaries, increasing the contact angle and height; but the coverage remains almost unchanged after reaching the equilibrium state. Further increasing the overpotential leads to the increase of the NB curvature (potential shift), as well as a higher gas outflux rate, namely, higher background current. As confirmed by molecular dynamics simulations, the "pin-rise" growth mode and the quantitative influence of NBs on the electrochemical performance have been revealed.

Broader context

Electrochemical gas evolution reactions (GERs) often suffer from large overpotentials before visible bubbles emerge, which is widely acknowledged to be initiated by the formation of interfacial nanobubbles. However, according to this traditional view, bubble formation should have a high nucleation barrier and a rapid barrier-less growth process, which is contradicted by the experimental observation that a higher overpotential is required for enlarging the NBs to visible ones. Here, for the first time, we resolve this contradiction by observing the "pin-rise" growth mode of interfacial nanobubbles under electrolysis conditions with the combination of newly developed SPRi technology, atomic force microscopy, and molecular dynamics simulations.

1. Introduction

Electrochemical gas evolution reactions (GERs) play vital roles in energy storage and chemical production,[1-4] *e.g.* water splitting rections[5,6] and in the chlor-alkali[7] industry. For a typical process, it is widely acknowledged that the generated gas products evolve from nanobubbles (NBs) on defects (*e.g.*, cracks or crevices) at the electrode surface, which then grow in size (commonly >20 µm) until the buoyancy force peels them off from the electrode.[8] To lower the overpotential, which is the key

to determining the device's energy efficiency, tremendous efforts have been devoted to developing catalysts with efficient intrinsic activity.[9-14] Meanwhile, electrode structure engineering (*e.g.*, nanoarray-based superaerophobic electrodes) has recently attracted attention for enhancing the current density per overpotential voltage.[15] This is because the interfacial bubbles formed during the GERs can block the effective contact between the electrolyte and the electrode surface, thereby hindering the mass transfer and decreasing the system conductivity, leading to a decrease in energy efficiency.[16,17]

Before phase transformation into macroscopic bubbles, interfacial NBs would bring unexpected impacts on the electrochemical overpotential after nucleation. According to the Young–Laplace equation ($\Delta p = \frac{2\gamma}{r}$, γ is the surface tension; r is the bubble radius), the internal pressure of bubbles is inversely proportional to their radius, indicating that the ultra-small sized NBs would adopt an extremely high internal pressure (*e.g.*, ~ 28 bar for 50 nm NBs).[18] In this context, one can deduce that the increase of the bubble size (radius) during the growth of NBs would lower the internal pressure and consequent chemical potential of NBs.[19]

[a] *State Key Laboratory of Chemical Resource Engineering, Beijing University of Chemical Technology, Beijing 100029, China. E-mail: luoliang@mail.buct.edu.cn, sunxm@mail.buct.edu.cn*

[b] *Beijing Advanced Innovation Center for Soft Matter Science and Engineering, Beijing University of Chemistry Technology, Beijing 100029, China. E-mail: hli@mail.buct.edu.cn*

[c] *Department of Chemistry, Tsinghua University, Beijing 100084, China*

† Electronic supplementary information (ESI) available. See DOI: https://doi.org/10.1039/d2ee04143j

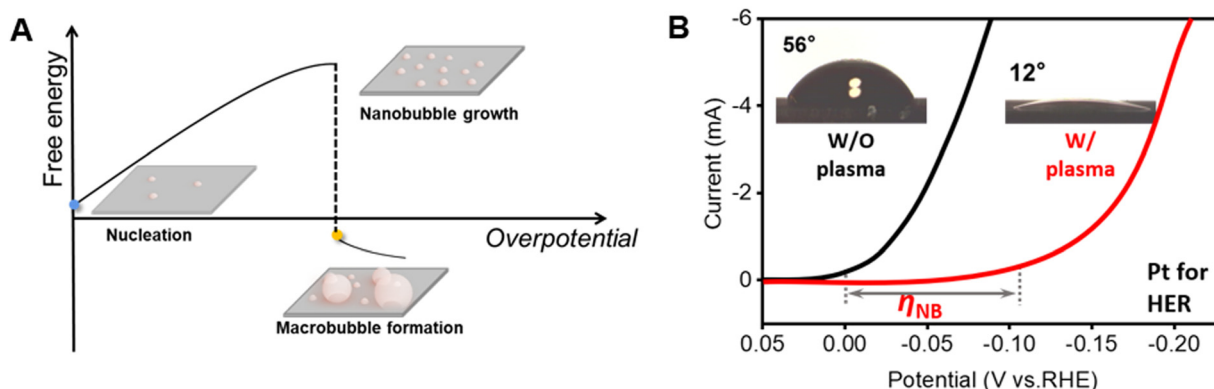‡ These authors contributed equally to this work.

Fig. 1 (A) Schematic illustration of the relationship between the free energy of the electrode surface bubbles and the overpotentials during gas phase transformation. (B) Linear sweep voltammetry curves (LSVs) of the HER with (the red line) and without (the black line) oxygen plasma treatment. An additional initial overpotential (η_{NB}) emerges after oxygen plasma treatment.

In other words, after overcoming the rate-determining nucleation step, the further growth of NBs should be a smooth, fast and even accelerated process. However, a higher overpotential is required to complete the gas phase transformation from NBs to macroscopic bubbles (Fig. 1A), as evidenced by the monotonic increase of the current density with the overpotential in common polarization curves. That is, the transformation of NBs into macroscopic bubbles would require higher free energy (ΔG) to overcome a critical value, which still remains a mystery.

As is well known, the growth kinetics of macroscopic bubbles can be investigated using a high-speed camera by recording the time-dependent variations of the radius, typically expressed by Scriven's theory as $R(t) = \beta t^x$,[20] where β stands for the growth coefficient and x represents the time coefficient. However, owing to their ultrasmall size,[21–24] the growth of interfacial NBs is usually considered to be governed by inertia imposed by the nearby liquid in milliseconds,[25] exhibiting ultrafast kinetics as turning into macroscopic bubbles, accompanied by the reduction of free energy. In pioneering studies, White et al. investigated the nucleation of single embryo NBs by recording the variation of current based on individual nano-sized model electrodes, gaining insights into the NB's critical nuclei size, reaction rate and activation energy, supersaturation in solution, etc.[26–29] Nakabayashi et al. verified the formation of surface NBs and the resultant potential shift during electrochemical reactions.[30] However, the chemical potential of NBs is significantly associated with morphological characteristics such as geometry (e.g., radius, height, contact angle, and curvature) and the surface coverage of electrodes. Operando detection with a sufficient spatial and temporal resolution is highly desirable. Yet, to overcome the limitation of the sampling time and statistics of classic atomic force microscopy (AFM) technology,[31,32] several in situ optical imaging technologies such as total internal reflection fluorescence microscopy (TIRFM)[33] and dark field microscopy (DFM)[33] have been developed to track the evolution dynamics of NBs,[34,35] demonstrating the potential of fast imaging of optical systems.

In this study, a surface plasmon resonance imaging (SPRi) technique, which is extremely sensitive to the dielectric field change, and widely used in biological binding/recognition studies,[35–37] is employed to investigate the formation and growth of interfacial NBs using the hydrogen evolution reaction (HER) as a probe. An operando real-time observation system is set up with a Pt/Au nano-film as both a working electrode and a plasmonic imaging platform, where the SPR reveals the growth of NBs statistically by showing increased reflectivity, and AFM yields images with a high spatial resolution for each NB (e.g., pinning states and curvatures). It is observed that NBs originate from pancake shaped ones, and then inflate with pinned three-phase boundaries, leading to the increased bubble contact angle (CA) and height, reduced curvature radius, and higher chemical potential of the gas inside the NBs. Such higher chemical potential results in higher supersaturation of vicinal dissolved gas and a greater background current, as a consequence of increased overpotentials. And this process is further confirmed by molecular dynamics (MD) simulation. The present work not only provides a promising method to track the real-time growth of interfacial NBs, but also uncovers the crucial role of NBs in determining the efficiency and the overpotential of GERs, and may inspire further optimization for the phase transformation of electrode surface NBs.

2. Materials and Methods

Electrochemical SPRi (EC-SPRi) setup

Electrochemical SPRi (EC-SPRi) was conducted to explore the behaviors of nanobubbles, and the experimental setup was based on the Kretschmann configuration, as shown in Fig. 2A. Polarized incident light (808 nm) was directed onto a gold film via a BK7 quartz prism, and the reflected light was imaged with the objective. At the same time, an SPR response (variation of reflectivity) from the totally inner reflected light was obtained. The electrochemically deposited Pt on the surface of an Au-coated prism was used as the working electrode, a carbon rod as the counter electrode, and a saturated calomel electrode as the reference electrode to fabricate a three-electrode in situ electrochemical reaction cell. As the sensitivity
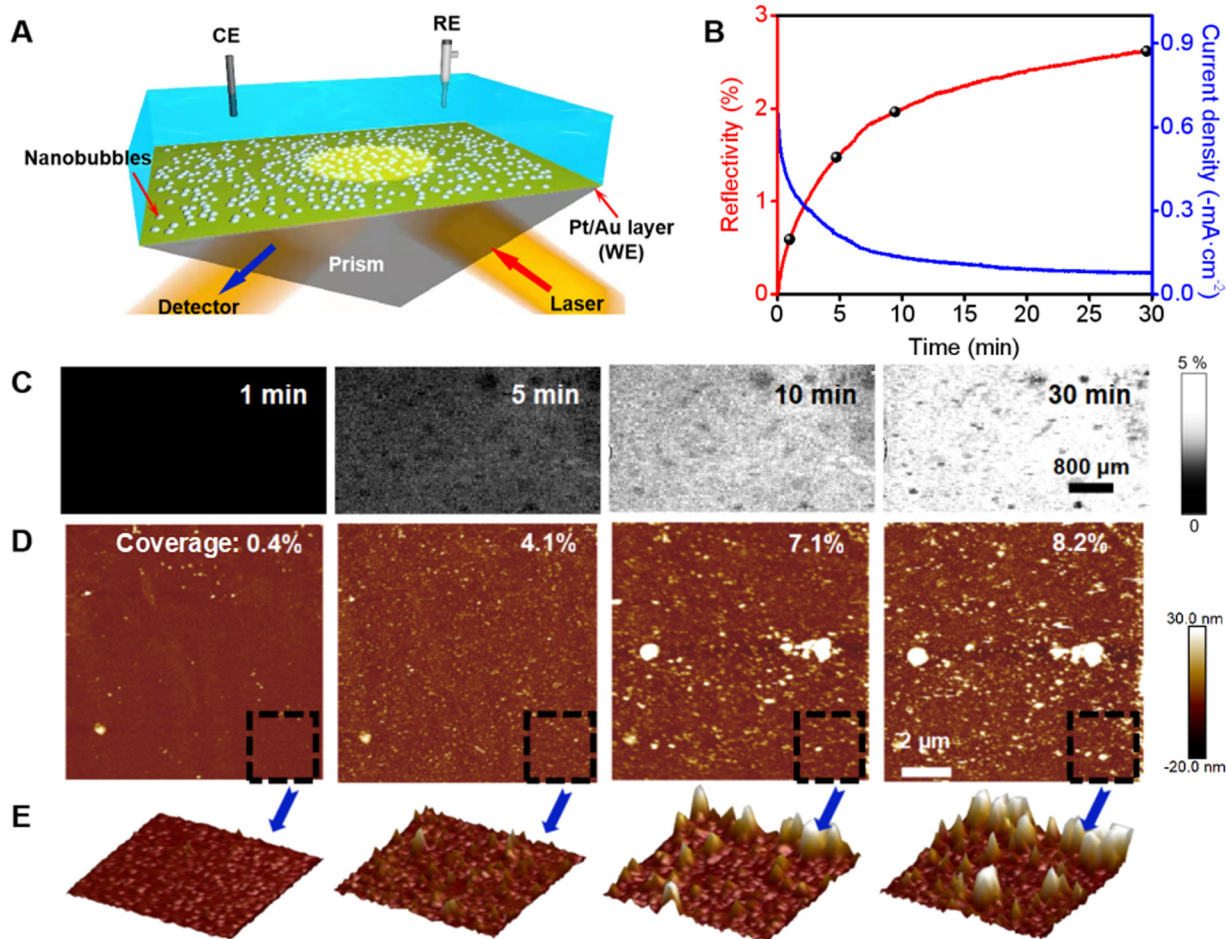
Fig. 2 Time-dependent evolution of NBs at an overpotential of 50 mV. (A) Schematic diagram of the experimental setup for the electrochemical surface plasmon resonance imaging (EC-SPR). (B) Time-dependent SPR reflectivity (red curve, left axis) and current density (blue curve, right axis). (C) SPR, (D) AFM, and (E) 3D views of AFM images captured at 1, 5, 10, and 30 min during the hydrogen evolution reaction.

of the SPRi technique is highly dependent on the dielectric constant, the deposited amount of Pt should be very small to minimize the dielectric constant variation of the original plasmonic Au film. As revealed by SEM (Fig. S1B, ESI†) and AFM images (Fig. S2, ESI†), no obvious Pt nanoparticles were formed and no obvious color change was observed after Pt deposition. The elemental mapping and onset potential comparison of linear sweep voltammetry (LSV) curves for Au (−0.1 V *vs.* RHE) and Pt/Au (0 V *vs.* RHE) electrodes (Fig. S1A, ESI†) verify the successful decoration of Pt on a Au film. The influence of dielectric constant variation for SPRi sensing with Pt and without Pt coated prisms was further evaluated by measuring the reflectivity at different potentials (−0.4 to 0.7 V) (Fig. S3, ESI†). There is a potential-dependent variation of reflectivity, which might result from the dielectric constant change induced by the modulation of free electrons of the metal film at different potentials, but the very limited deviation between the two reflectivity curves (Au and Pt/Au) indicates that the dielectric constant remains nearly the same after the atomic level deposition of additive metals on the Au film.

An electrochemical HER test was performed in 0.05 M H$_2$SO$_4$ solution with a scanning rate of 5 mV s^{-1}, with a saturated calomel electrode as the reference electrode, and a platinum electrode as the counter electrode.

Verification of the ultra-sensitivity toward gas molecules

Before the experiment, we assessed the theoretical reflectivity with polarized incident light (R_{p}) of gas molecules. The theoretical reflectivity change can be calculated using eqn (2),[38]

$$R_{p} = |r_{012}|^2 = \left| \frac{r_{01} + r_{12}e^{2ik_{y1}d}}{1 + r_{01}r_{12}e^{2ik_{y1}d}} \right|^2 \qquad (2)$$

where r represents the reflection coefficient between the two layers; 0, 1, and 2 represent the prism, gas, and electrolyte, respectively.

The reflection coefficient (r) between two interfaces is given using eqn (3),[38]

$$r_{ij} = \frac{\varepsilon_j k_{yi} - \varepsilon_i k_{yj}}{\varepsilon_j k_{yi} + \varepsilon_i k_{yj}} \qquad (3)$$

where k is the longitudinal wave vector, and ε is the dielectric constant of different layers (y and j are quartz and Au,

respectively). Here, the dielectric constants of quartz and Au are 2.25 and −16, respectively.

Furthermore, the k value can be calculated using eqn (4),[38]

$$k_{yj}^2 = n_i^2 \, (2\pi/\lambda)^2 \, ((n_j^2)/(n_i^2 - \sin 2\alpha)) \tag{4}$$

where n_i and n_j are the refractive indices of the prism (1.515) and Au (1.48), respectively.

Accordingly, the theoretical reflectivity (R) change of gas molecules was calculated to be 36.6%, which is an extremely big value, and directly related to the sensitivity toward gas bubbles. To demonstrate the considerable reflectivity change, we compared the SPR curves of the evolution of a single hydrogen bubble on a Pt/Au film prism and reference biomolecule (DNA) recognition (Fig. S4, ESI†). As the bubble grows and finally fully occupies the pre-selected area as marked in a red circle (Fig. S4, ESI† inset), the reflectivity gradually increases and reaches a plateau of ∼36%, while the reflectivity of similarly fully occupied DNA molecules is only about 7%. Similarly, the corresponding SPR images (Fig. S4, ESI† inset) also display that the contrast of the bubble contact area is much higher than the binding area of DNA molecules. This suggests that the SPR is suitable for bubble observation.

Characterization of surface nanobubbles

SPR (Horiba) and AFM (Bruker catalyst) were used to characterize the geometric change and growth trend of surface nanobubbles in the electrochemical gassing reaction. SPR is very amenable for studying the nanobubble system due to its very high response degree, and the change in the nanobubble on the electrode can be judged according to the changing trend of the image. AFM is a traditional instrument used to characterize nanobubbles. As shown in Fig. S5 (ESI†), tip correction (the AFM probe scans a given patterned substrate and compares the obtained groove size with the standard size) was used to improve accuracy, and the tapping mode is used to obtain the geometry of surface nanobubbles.

Simulation methodology

A patterned plate with 4 layers of Au was utilized as the substrate in the simulation. Au atoms of different color were assigned different interaction parameters to simulate heterogeneous nucleation as shown in Table S1 (ESI†).[39–42] The size of the whole simulation box is 14 nm × 14 nm × 12 nm. Molecular dynamics simulations are performed with a modified version of the open source code LAMMPS.[43] The equations of motion are integrated with the velocity Verlet algorithm with a time step of 5 fs. The temperature is set to 300 K, controlled with the Nose–Hoover thermostat with a relaxation time of 0.25 ps.

The electrochemical production of gas at the electrode is mimicked by inserting it at a random position within a disk with the same area of the electrode and 2.5 Å above the Au electrode. The gas molecules can only be created if there is at least one water molecule within 4 Å of the creation point, because water is needed for the electrochemical reaction to proceed in the experiment. If that requirement is not met, a new gas creation attempt elsewhere above the electrode plane is carried out for the same configuration, up to ten trials. The gas molecules' inserting frequency (F) was used to mimic the electrochemical reaction driving force by using the algorithm.[44] With the different values of F, we can get the variations of the NB profile and internal pressure P_{NB},

$$P_{NB} = \frac{Nk_B T}{V} + \frac{\sum_i^N r_i \cdot f_i}{dV} \tag{5}$$

where N is the number of atoms in the selected calculation region, V is the volume of the calculation region, k_B is the Boltzmann constant, d is the dimensionality of the system, and r_i and f_i are the position and force vector of atom i, respectively.

The whole simulation box was split into several cubic meshes with a size of 3 Å, and the local water density in each mesh was recorded. By plotting the half-water-density points as the NB profile, we can obtain the CA.

3. Results and discussion

Operando observations of interfacial NBs at an overpotential of 30 mV

We conducted electrochemical HER measurements using a Pt deposited Au film with mild hydrophilicity (CA = 56°) as the working electrode. Similar to those typical polarization curves, the overpotential losses can be divided into three parts[25,45,46] (Fig. 1B): activation overpotential (η_a),[16,47] ohmic overpotential (η_{Ohm}),[48,49] and concentration overpotential (η_{conc}).[45,50,51] However, as the electrode surface was treated with oxygen plasma to strengthen the hydrophilicity until the water droplet CA dropped to 12° (Fig. 1B inset), an obvious extra HER overpotential of ∼100 mV, as compared with the electrode without oxygen plasma treatment, is added. By contrast, as the reaction switched to non-bubble redox of potassium ferricyanide on two identical electrodes with/without oxygen plasma treatment, the two reduction curves overlap each other perfectly (Fig. S6, ESI†), verifying that the extra overpotential should be related to new (gas) phase formation. We defined this extra overpotential as η_{NB}, which is the nanobubble-induced overpotential during the initial stage of gas evolution reactions.

Various increasing overpotentials from 50 mV to 200 mV (*vs* RHE) with an interval of 50 mV were applied on the oxygen plasma treated Pt/Au electrode to check the bubble effect. As shown in Fig. S7 (ESI†), there are no macroscopic bubbles on the electrode surface at small overpotentials (50 and 100 mV), and the current decreases exponentially to a smooth and rather limited balanced value lower than 1 mA cm^{-2}. While the balanced current becomes fluctuant as the applied overpotential is set to 150 mV, accompanied by macroscopic bubble formation on the electrodes. With a further increased overpotential at 200 mV, more macroscopic bubbles are generated on the electrode, whose growth and detachment further induce strong current fluctuations.

The above "current fading" experimental phenomenon should be relative to the NB formation at the electrode/electrolyte

interface before the appearance of macrobubbles in a relatively large potential window (nearly 100 mV) after oxygen plasma treatment.[52] To gain further deep insights into the interface behaviors of the electrode/electrolyte, SPR technology, a method with high sensitivity to a dielectric constant change at the nanoscale,[53–56] was applied to investigate the "invisible" NBs at the surface of the Pt/Au prism electrode after careful verification (Fig. S1, ESI†). And, the applied overpotentials are restricted to lower than 100 mV to avoid visible bubble formation.

The experimental setup of the electrochemical SPR (EC-SPR) was established based on the Kretschmann configuration[57] to explore the behaviors of NBs (Fig. 2A). The polarized incident light (808 nm) was directed onto the Pt/Au film *via* a BK7 quartz prism, and the reflected light was imaged with the objective. At the same time, an SPR response (variation of reflectivity) from the totally inner reflected light was obtained. A considerable change in the reflectivity from the SPR image, which is tightly related to the dielectric constant, is observed due to the formation of a new gas phase. And then the reflectivity change could indicate the bubble-coverage ratio finally. The control experiment was conducted in a certain area totally covered by a planted macrobubble, and the reflectivity can reach up to a maximum value of $\sim$36%, which is also in accord with the theoretical calculation (SI), which is much higher than that of totally covered by the commonly applied DNA molecules (7%). Therefore, the variation of the reflectivity of SPR of the generated NBs from the totally inner reflected light can be regarded as a bubble-coverage ratio.

After the oxygen plasma treatment of the electrode, as conducted at an overpotential of 30 mV (-30 mV *vs.* RHE electrode) with a scanning rate of 5.0 mV s^{-1} in 0.05 M H$_2$SO$_4$ solution, the current density rapidly decreases in 5 min and gradually reaches a plateau after 20 min (Fig. 2B), accompanied by the brightening of typical SPR images of the whole prism (Fig. 2C), as well as a fast increase of reflectivity reaching up to $\sim$3%, which implies the formation of NBs with a coverage of nearly 8% on the electrode (100% $\times$ 3%/36%).

As combined with statistical SPR imaging, we collected *in situ* time-dependent AFM images on a hydrophilic electrode within a 10 $\times$ 10 μm^2 area under the same reaction conditions (Fig. 2D) to source the time-dependence function of the current density and reflectivity. Profile details of each NB, including the height and the contact area can be obtained by AFM after tip-correction, which was conducted by scanning a standard substrate with a given size (280 $\times$ 200 nm^2), and the clear image verifies the tip precision (Fig. S5, ESI†). Before the reaction, the roughness of the Pt/Au surface was verified as low as 1.3 nm (Fig. S2, ESI†). In the beginning of the reaction ($\sim$1 min), there were a few tiny white spots accounting for only 0.4% coverage (the ratio of the total contact area of NBs to the electrode area.) in the whole area, which were further confirmed as NBs after brief AFM scanning by showing a negative signal compared with the Pt/Au substrate in the force profile (dim spots in Fig. S8, ESI†).[58] As the working time is prolonged from 1 to 30 min, the coverage of NBs increases from 0.4% to 8.2%, as

evidenced by the 3D-view AFM images (Fig. 2E), with some NB agglomerates (Fig. S9, ESI†). The evolution of the NB coverage is increased quickly to a plateau, consistent with the variation of the current density and the reflectivity of SPR images (Fig. S10, ESI†). Accompanied by the continuous formation of NBs on the electrode surface, the current density reaches an equilibrium value of 0.083 mA cm^{-2}.

Operando observations of equilibrium interfacial NBs at different overpotentials

Next, various overpotentials (10 mV to 50 mV) were applied on the electrode to reveal the variations of the current density and SPR reflectivity (Fig. 3A and B) during the HER process. As it is conducted at a overpotential of 10 mV for 10 min, the system tends to approach a dynamic equilibrium state with a current density of 0.047 mA cm^{-2} and a reflectivity of 1.4% after an initial rapid decrease of the current density and an increase of reflectivity. As the applied overpotential increases, both the current density and the reflectivity rapidly reach the corresponding new plateaus (current density plateaus of 0.050 to 0.069, 0.095, and 0.157 mA cm^{-2}, corresponding to the given overpotentials of 20, 30, 40, and 50 mV, respectively). Accordingly, the reflectivity exhibits the same rising trend (from 1.5% to 1.7%, 2.0%, and 2.7%) as that of the current density (Fig. 3C). This indicates that each overpotential can supply a certain driving force to form NBs with a given curvature, and enable a new balanced state with an equilibrium current density. After normalizing the time-dependent current variations (Fig. S11, ESI†), it can be found that the current density reaches equilibrium at essentially the same time at different overpotentials, as well as the changing trend of current density (Fig. S12, ESI†). Correspondingly, the brightness of SPR images of the equilibrium states also rises faster with an increase of the overpotential but terminates at the same time point (Fig. 3D). As revealed by the top-view and 3D-view AFM images (Fig. 3E, F), the coverage of equilibrium NBs surprisingly remains nearly constant as 7% $\pm$ 1% at different overpotentials, besides more agglomerates appear at higher overpotentials (*e.g.*, 50 mV), which indicates that the brightening of SPR images would be mainly attributed to the variation of the NB morphology/height.

In the SPR configuration, the excited evanescent wave usually propagates tens of micrometers in the lateral direction, and thus the reflectivity is sensitive to the interfacial variation. As there are species adsorbed or generated on the given surface, the localized evanescent wave would be greatly attenuated and the reflectivity would increase. By contrast, in the vertical direction, the evanescent wave is exponentially damped away from the interface (Fig. S13A, ESI†), so that the reflectivity is not sensitive to the height of NBs, except for the bubble edge. For the cap-shaped surface NBs, their edge region has a rather small height, usually lower than 10 nm, and the edge part of the evanescent wave would be partially attenuated, not as fully as the central part (Fig. S13B, ESI†). As a result, when interfacial NBs further grow with an increase of the contact angle, the edge part would be thickened, and the corresponding localized
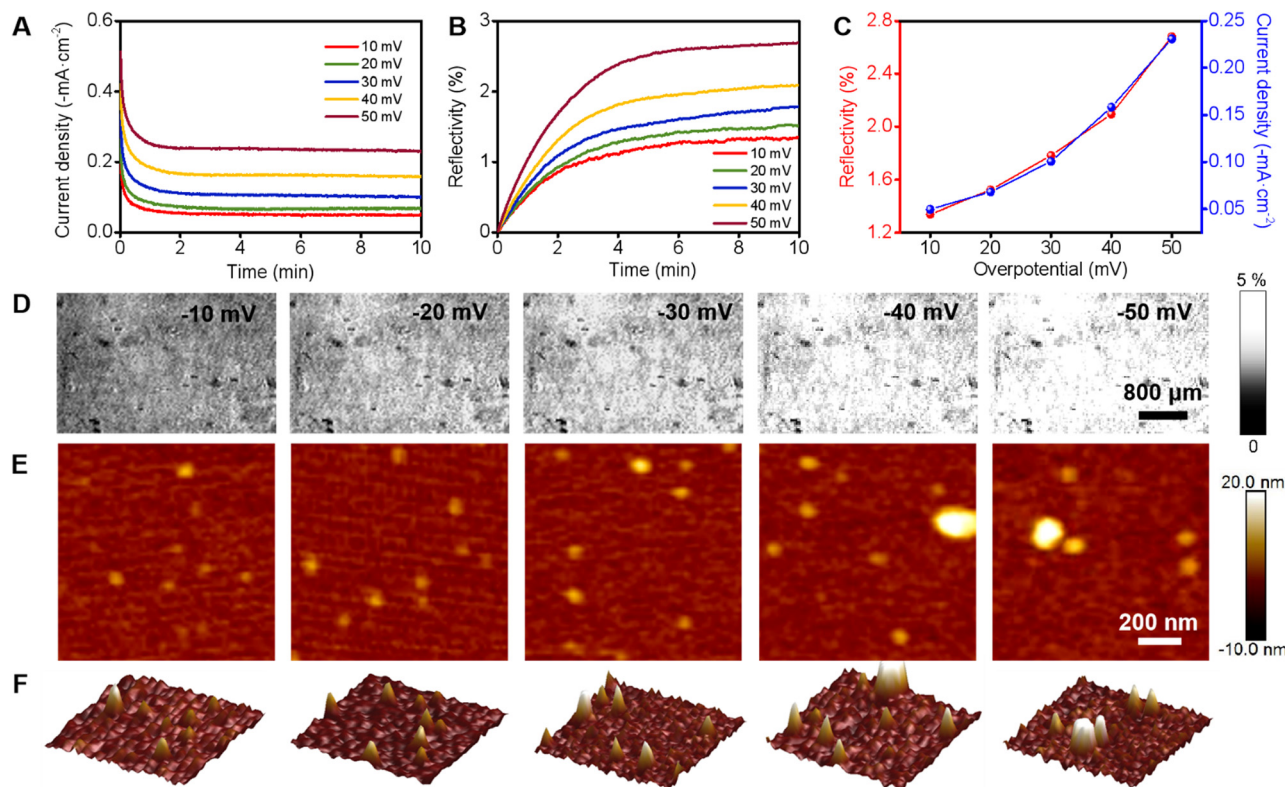
Fig. 3 Overpotential-dependent variations of nanobubbles. (A) Current density and (B) reflectivity of SPR of Pt/Au electrodes, as a function of time at varying overpotentials: 10, 20, 30, 40, and 50 mV. (C) Curves plotting the reflectivity (red dots) and equilibrium current (blue dots) as a function of the overpotential. Overlapping of the 2 lines indicates the strong relationship between the two factors. (D) SPR, (E) AFM, and (F) 3D-view of AFM images captured at −10, −20, −30, −40 and −50 mV during the HER in the plateau zone of SPR.

evanescent wave would be further attenuated slightly, leading to a limited increase of reflectivity (Fig. S13C, ESI†).

Variations of interfacial NBs during the growth process and equilibrium states

Deep analysis of AFM measurements was applied to obtain more detailed structural parameters of NBs to reveal how the SPR images become brighter under the same bubble coverage. As shown in Fig. 4A and 4B, with the height (H) and the contact diameter (D), the curvature radius (r) of the NBs can be calculated using the equation $r = \dfrac{H^2 + D^2/4}{2H}$, and therefore the bubble CA can also be obtained. Typically, at a constant overpotential of 30 mV, a few embryo NBs nucleate stochastically on the electrode surface within 1 min, as an initial pinning stage with an average CA of $\sim 26°$ (H = 7 nm, D = 62 nm, and r = 74 nm, corresponding to 19.5 bar). Subsequently, massive NBs form in the next 5 min, and the size and shape of NBs also change rapidly to reach a CA of $\sim 45°$ (H = 13 nm, D = 72 nm, and r = 51.5 nm, corresponding to 28 bar). As the reaction time is extended to 30 min, the coverage of NBs approaches a constant value of 8.2% (Fig. 2D), and the morphology also stabilizes (CA = 47°, H = 15 nm, D = 74 nm, and r = 51.5 nm, corresponding to 28 bar), indicating the dynamic equilibrium state. This analysis indicates that the interfacial NBs grow

rapidly with the fast increasing CA (from 26° to 45°) and H (from 7 to 15 nm), but limited the change in D (from 62 to 74 nm) at a given overpotential, which is higher than that required for NB nucleation. Namely, the three-phase boundaries move outward a little within the first 8 min, then reach a dynamic equilibrium state with a constant morphology and pinning contact lines. The curvature indicator, r, decreases rapidly in the beginning and approaches a plateau in the end (from 74 to 51.5 nm) as evidenced by the time-dependent statistics of AFM measurement (Fig. S14, ESI†). It should be noted that the constant contact diameter (CCD) mode is also nearly applicable to describe the NB growth features, where the diameter only expends from 62 nm to 72 nm (16%) while the height is increased from 7 nm to 13 nm (nearly 2 times). It is also closely related to the "rising-up" growth mode, which bridges the growth behaviors of NBs and the impact on overpotential, based on the well-known characteristic CCD mode.

According to the statistics of the NB dynamic equilibrium states at different overpotentials from 10 to 50 mV (Fig. S15 and S16, ESI†), the average values of CA gradually increase from 40° to 65°, and H simultaneously climbs from 10 to 19 nm, while D only slightly varies from 64 to 68 nm. This indicates a stricter, nearly CCD variation mode of the NBs with their three-phase boundaries steadily pinning on the surface (Fig. 4C and D) than the time-extension case. This CCD evolution mode leads to a
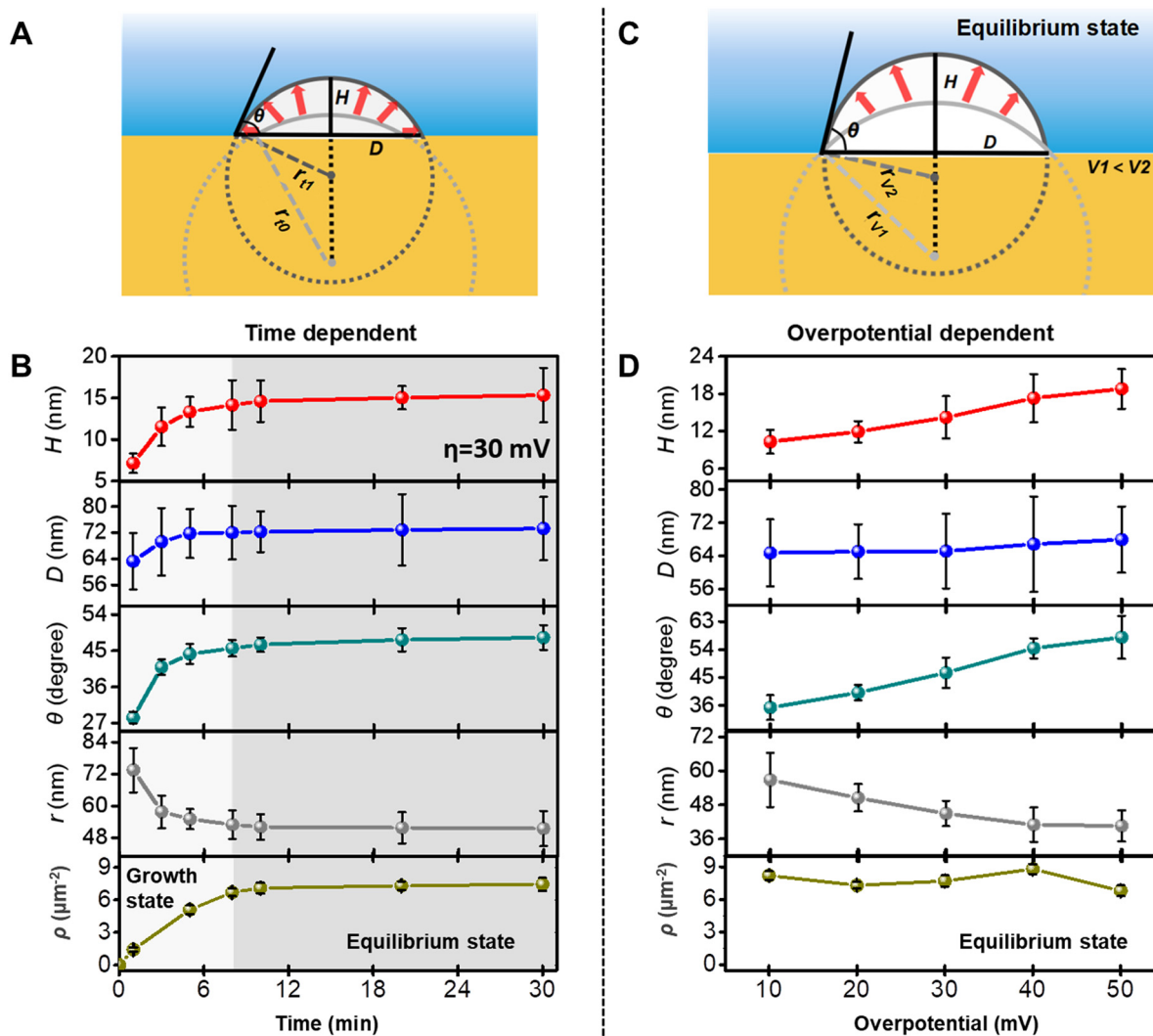
Fig. 4 Time- and overpotential-dependent growth model of the formed nanobubbles by analysis of AFM characterization. (A) Schematic illustration of the time-dependent growth model of nanobubbles. (B) Time-dependent variations of the contact angle (θ), height (H), contact diameter (D), curvature radius (r) and number density (ρ) of NBs at 30 mV. (C) Schematic illustration of the overpotential-dependent growth model of the nanobubbles. (D) Overpotential-dependent variations of the height (H), contact diameter (D), contact angle (θ) and curvature radius (r) and number density (ρ).

decrease of r from 56 to 40 nm. Correspondingly, the internal pressure of NBs would be increased by $\sim 40\%$ according to Laplace pressure calculation. It explains the reason why η_{NB} is much more obvious after oxygen plasma treatment: the plasma treated Pt/Au surface is of higher hydrophilicity, which means that the extension of bubble zones or movement of the contact line into the liquid phase would be more difficult (Fig. 1B). As the surface is confirmed by the variations of the SPR images and the curves with different oxygen plasma treatment times, NBs are more likely to be retained on the electrode surface with higher hydrophilicity (aerophobicity) (Fig. S17, ESI†).

Moreover, it is further found that the change in coverage is rather limited ($<1.5\%$) at various overpotentials (10–50 mV, Fig. S18, ESI†), and the number density (ρ) of NBs is almost unchanged (Fig. 4B and D), indicating that the increased overpotential prefers to promote the "pin-rise" growth of formed NBs rather than new bubble nucleation. Such constant ρ would

induce balanced distribution and distance between the NBs. If new NBs are formed, the shortened distance between the already formed NBs and newly formed nuclei would promote the interactions of gas molecules between the adjacent NBs, namely, ripening.[59] As a result, the reflectivity variation and the brightening of the SPR images (Fig. 3B and D) at different overpotentials can be mostly attributed to the increase of bubble height, as the evanescent wave on the Pt/Au surface can be extended to a height of ~ 200 nm based on an applied polarized incident laser of 808 nm in principle (Fig. S13A, ESI†).[60] The results reveal that the equilibrated geometry of the formed interfacial NBs tightly depends on the applied overpotential: the higher applied overpotential causes a higher chemical potential of the electrochemically generated gas, corresponding to the higher internal pressure of the formed interfacial NBs (with a smaller curvature radius).

Since the *operando* electrochemical cell in our experiments can be regarded as an open system without sealing, the high

pressure inside NBs (26–36 bar) would lead to supersaturated environments which release H_2 into the bulk solution besides into bubbles. Thus, the decrease of the r value at a higher overpotential would increase the concentration gradient between the interfacial NBs and the bulk aqueous phase, thereby enhancing the outflux of H_2 from NBs to the bulk phase, to generate overpotential-dependent residual current (Fig. 3A and Fig. S19, ESI†). When the applied potential is further increased over the threshold, the over-high internal pressure caused by a greater CA will eventually cause the sudden expansion of the three-phase contact line (*i.e.* de-pinning), which breaks the dynamic equilibrium between the chemical potential of NBs and the applied overpotential (and residual current). The depinning is accompanied by a sudden increase of the bubble radius and a significant decrease of the gas chemical potential, leading to accelerated generation of massive amounts of gas and rapid extension of NBs and formation of macroscopic bubbles.

Simulations of variations of interfacial NBs

To uncover the molecular mechanism of the surface pinning effect in NB growth on a flat electrode surface during the GERs, as well as the corresponding relation between the NB geometry and the overpotential, atomistic molecular dynamics (MD) simulations are carried out to investigate the interfacial NB formation process using an algorithm to mimic the driving force (*i.e.*, electrochemical overpotential) with the frequency F of gas creation attempts.[35,44,61] The whole simulation system is divided into three regions: the empty reservoir, the electrolyte layer, and the substrate with a cylindrical hydrophobic region (bubble-generation region) with weaker interaction parameters, as well as the surrounding hydrophilic region with stronger interaction parameters.[44,62] On a real electrode surface, due to

the heterogeneous chemical compositions, surface roughness, and impurities' adsorption, the non-uniform distribution of wettability is inevitable. It is noteworthy that in experimental studies, it was found that the NBs tend to form on aerophilic spots. In order to mimic the real electrode surface for NB growth, we constructed a heterogeneous electrode (as shown in Fig. 5A), consisting of a yellow hydrophobic region for nucleation and a gray hydrophilic region for the de-pinning limitation of the three-phase contact lines. Their hydrophilicity was regulated by the parameter in the Lennard-Jones potential.

After the full relaxation of the whole system without any gas molecules, we start the generation of H_2 molecules by applying a certain driving force $F = 0.4$ ps^{-1} (one reaction attempt for every 2.5 ps), and the formation process of the NB is shown in Fig. 5A. Fig. S20 (ESI†) shows that the nanobubble fully reaches a stable state after 10 ns. MD simulations show rapid nucleation of NBs on the hydrophobic region of the electrode, where the dissolved H_2 molecules tend to gather on the surface and show a pancake morphology, coinciding with experimental results in Fig. 2D to show easy initial nucleation of the interfacial NBs. Then, the initial growth of the NBs follows a triple-line-extension mode with a super large CA until the pancake gradually occupies the whole hydrophobic area of the electrode. After that, the contact line of the NBs is pinned by the hydrophobic/hydrophilic boundary, and the growth of the NBs starts to follow a CCD mode, with the CA and the bubble height being gradually increased by the continuous injection of H_2 molecules. Meanwhile, accompanied by an increase of CA, the growth rate of the NBs becomes lower and gradually approaches 0, and finally stops with a CA close to 90°,[63] which is almost the same degree on different sized substrates (Fig. S21, ESI†). By comparing the CAs and curvature radii with
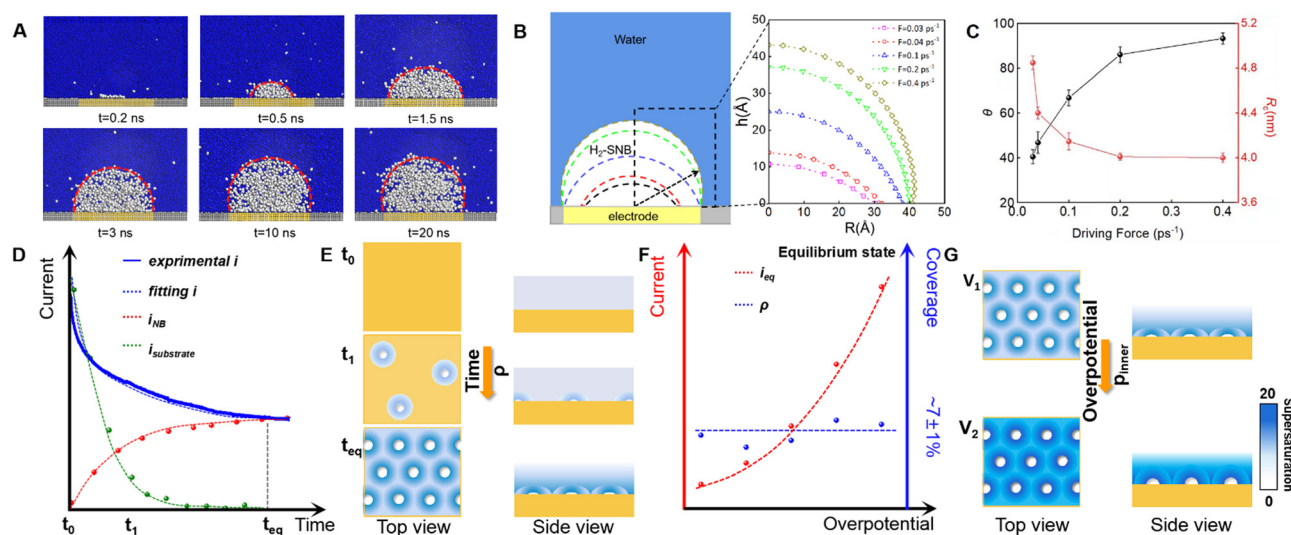

Fig. 5 Simulations and electrochemical verification of interfacial H_2 NBs. (A) Snapshots of the nucleation and growth of a H_2 NB on an electrode surface when the gas creation frequency $F = 0.4$ ps^{-1}. (B) Schematic diagram of the growth of a NB on the Au electrode surface and the shape of NBs with different driving forces. (C) The contact angle of the NB and curvature radius of the NB corresponding to the different driving forces. (D) The time-dependent current variation of the diffusion, the free area and the sum of them. (E) Schematic illustration of the time-dependent NB growth process at a certain overpotential. (F) Variation of the coverage and equilibrium current at different overpotentials. (G) Schematic illustration of the overpotential-dependent NB growth process.

different driving forces (Fig. 5B and C), it is confirmed that the equilibrated CA and the curvature radius of the pinned NBs are respectively increased with the increase of driving force (applied overpotential). However, we also find that the curvature radius and contact angle of the nanobubble have critical values within a certain range of driving force (Fig. S22, ESI†) Furthermore, the higher internal pressure of NBs at higher overpotentials was also confirmed by MD simulations (Fig. S23, ESI†). Therefore, the simulated growth process of NBs is consistent with the experimental observations and previous predictions.[64]

Based on the experiments and simulations, a time-dependent bubble-current model is proposed to quantify the relation between the residue current and the NB morphology and coverage (Fig. 5D). For a typical process at a certain overpotential, the electrochemically generated H_2 molecules based on such an unblocked area would mainly contribute to new nucleation of NBs and/or growth of already formed NBs (defined as "$i_{substrate}$", green line) and the replenishment of the above-mentioned outflux of NBs (defined as "i_{NB}", red line),

$$i = i_{substrate} + i_{NB} \quad (6)$$

At the beginning (defined as t_0), there is no NB formed on the electrode, the contribution to the current i (blue line) is solely the exposed electrode substrate (green line). After that, with the free nucleation/generation of NBs (t_1), the unblocked area significantly decreases, with the opposite variation trend of NB coverage (ρ), thereby the corresponding current contribution can be expressed as

$$i_{substrate} \propto d\rho/dt \quad (7)$$

Meanwhile, a supersaturated gradient (Fig. 5E) would form near the surface of each NB. The supersaturated gradients near NBs would release H_2 molecules into the bulk solution (the outflux of H_2). According to Fick's Law,[65] the outflux rate (j) is determined by a supersaturated gradient, as $j = -D\nabla C_s$, where D is the gas diffusion coefficient and ∇C_s is the concentration gradient, which should be proportional to the concentration difference value between the surface concentration C_s and the bulk concentration C_0, namely, ($C_s - C_0$). By assuming the same concentration gradient nearby for each NB, the diffusion current for the replenishment of the total outflux diffusion of H_2 molecules into the bulk solution on the whole electrode can be expressed as

$$i_{NB} \propto \rho z FD(C_s - C_0) \quad (8)$$

where z is the electron transfer number, and F is the Faraday constant, respectively. Thus, at a certain overpotential, as the reaction continues (t_1), ρ and the CA are increased, and r is decreased (Fig. 4B), and as the supersaturated gradient ∇C_s increases, i_{NB} is correspondingly increased.

When the reaction prolongs to equilibrium state (t_{eq}) at a certain overpotential, the CA and ρ increase to a peak value without further variations over time, with the value of $d\rho/dt$ decreasing to nearly zero (Fig. S10, ESI†); Also, the supersaturated

gradients nearby each NB tend to be constant. Thus, the distribution of NBs can be approximately regarded a "close-packed" structure (Fig. 5E). In this case, $i_{substrate}$ decreases to nearly zero and i_{NB} reaches the maximum value.

For the equilibrium states at different overpotentials (e.g., 10–50 mv), the internal pressure of the NBs is proportional to the concentration according to Henry's law, namely, $P_{NB} = H \times C_s$, where H is Henry's coefficient. Thus, the applied overpotential can be balanced with the surface concentration of the NBs, as described according to the Nernst equation,

$$\eta = \frac{RT}{zF} \ln \frac{HC_s}{[H^+]^2 p^\theta} \quad (9)$$

where T represents the thermodynamic temperature, R is a constant, and $[H^+]$ is the proton concentration. According to the relative steady coverage of $\sim 7\% \pm 1\%$, in other words, the overall electrode surface can be considered as averagely divided by each NB, thereby we can infer that every NB would affect the surrounding zone about 14 times of NBs themselves. In contrast to the unchanged coverage, the NB profile (i.e., the CA and r) tightly associates with the surface concentration C_s (Henry's law), and hence the relationship between the equilibrium current (namely i_{NB}) and the applied overpotential can be revealed as combined with the Nernst equation,

$$i_{eq} \propto \rho \left[zFD[H^+]^2 p^\theta \exp\left(\frac{zF\eta}{RT}\right) \Big/ H - zFDC_0 \right]$$
$$= \rho[k \cdot \exp(A\eta) - B] \quad (10)$$

As the parameters except η can all be considered as the constants owing to the equilibrium state in a given system, the current exhibits an exponential function versus η with simplified constants k, A and B. The trend is in accord with the fitted curve (red line in Fig. 5F). As a result, a higher overpotential (η) endows the NBs with a higher internal pressure and higher surrounding supersaturation gradients (blue background in Fig. 5G, $V_1 < V_2$) according to the Young–Laplace equation, namely, higher outflux induced i_{NB} (red line in Fig. 5F), or a shorter time to the equilibrium state (Fig. S9, ESI†). In contrast, the results also indicate that interfacial NBs would generally grow up following a "pin-rise" mode with the three-phase contact line pinned, as well as varying profiles (CA and r) during the gas phase transformation process. Therefore, the as-formed NBs would indeed generate an extra overpotential for phase transformation into macroscopic bubbles, until the applied overpotential is large enough (e.g., >150 mV in Fig. S7, ESI†) beyond the critical value of the NB profile for extending ("de-pinning") the three-phase contact lines, which is determined by the electrode surface heterogeneity (such as type of materials, roughness, and surface wettability).[14] This underlines the importance of comprehensively understanding the NB growth process during gas evolution reactions, and may inspire further optimization for the phase transformation of electrode surface NBs, such as hydrophilic/hydrophobic hybrid electrode structures or surface tension tailoring (e.g., surfactants).

4. Conclusions

In conclusion, we carefully investigate the nucleation and growth process of interfacial H_2 NBs during the initial stage of the HER process using *in situ* SPRi, AFM, and MD simulations. A comprehensive picture of interfacial NB formation under the GER conditions has been revealed: (i) the nucleation of interfacial NBs on the aerophobic sites of the electrode surface is easy, while the further growth of NBs requires a higher applied overpotential. (ii) The growth of NBs exhibits a CCD mode with the three-phase contact line pinned by the surface heterogeneity. The "pin-rise" evolution of the interfacial NBs leads to a smaller curvature radius, higher Laplace internal pressure, and higher gas chemical potential, which endow the GERs with an extra overpotential η_{NB}. As compared to the growth of NBs, the nucleation of new bubbles on the hydrophilic surface is more difficult, and as a result, the surface coverage of NBs at different overpotentials remains almost unchanged. When the applied potential exceeds the critical profile value (CA or r) of NBs, the depinning of NBs occurs, leading to a sudden drop in gas pressure. Subsequently, the NBs rapidly expand into macrobubbles. Based on the data from *operando* SPRi and current measurements, we present a bubble-current model to establish the quantitative relation between the NB growth and the electrolysis current, which is a great step forward compared to the traditional Tafel current model for GERs. The present work not only provides a promising method to track the real-time growth of interfacial NBs, but also uncovers the crucial role of NBs in determining the efficiency and the extra overpotential during GERs, which sheds new light on electrode design for gas involving electrochemical reactions.

Author contributions

L.L. and X.S. designed the research; J.Y., Z.Z., Y.L., L.L. and X.S. performed the research; K.H. and H.L. performed the MD simulations; J.Y., Z.Z., Y.L., H.X., L.L., and X.S. analyzed the data; and J.Y., Y.K., H.D., F.W., K.H., L.L., H.L., and X.S. wrote the paper. All the authors discussed the results and commented on the manuscript.

Conflicts of interest

The authors declare that they have no competing interests.

Acknowledgements

References

1 Z. Lu, W. Zhu, X. Yu, H. Zhang, Y. Li, X. Sun, X. Wang, H. Wang, J. Wang, J. Luo, X. Lei and L. Jiang, Ultrahigh Hydrogen Evolution Performance of Under-water "Super-aerophobic" MoS_2 Nanostructured Electrodes, *Adv. Mater.*, 2014, **26**, 2683–2687.

2 Y. Li, H. Zhang, M. Jiang, X. Sun and X. Duan, Ternary NiCoP Nanosheet Arrays: An Excellent Bifunctional Catalyst for Alkaline Overall Water Splitting, *Nano Res.*, 2016, **9**, 2251–2259.

3 J. Deng, H. Li, S. Wang, D. Ding, M. Chen, C. Liu, Z. Tian, K. S. Novoselov, C. Ma, D. Deng and X. Bao, Multiscale Structural and Electronic Control of Molybdenum Disulfide Foam for Highly Efficient Hydrogen Production, *Nat. Commun.*, 2017, **8**, 1–8.

4 C. Tang, H. Wang and Q. Zhang, Multiscale Principles to Boost Reactivity in Gas-involving Energy Electrocatalysis, *Acc. Chem. Res.*, 2018, **51**, 881–889.

5 N. Suen, S. Hung, Q. Quan, N. Zhang, Y. Xu and H. Chen, Electrocatalysis for the Oxygen Evolution Reaction: Recent Development and Future Perspectives, *Chem. Soc. Rev.*, 2017, **46**, 337–365.

6 I. Roger, M. A. Shipman and M. D. Symes, Earth-abundant Catalysts for Electrochemical and Photoelectrochemical Water Splitting, *Nat. Rev. Chem.*, 2017, **1**, 1–13.

7 R. K. B. Karlsson and A. Cornell, Selectivity Between Oxygen and Chlorine Evolution in the Chlor-alkali and Chlorate Processes, *Chem. Rev.*, 2016, **116**, 2982–3028.

8 H. N. Oguz and A. Prosperetti, Dynamics of Bubble Growth and Detachment from a Needle, *J. Fluid Mech.*, 1993, **257**, 111–145.

9 M. Jahan, Z. Liu, K. P. Loh and A. Graphene, Oxide and Copper-centered Metal Organic Framework Composite as a Tri-functional Catalyst for HER, OER, and ORR, *Adv. Funct. Mater.*, 2013, **23**, 5363–5372.

10 J. Kibsgaard, T. F. Jaramillo and F. Besenbacher, Building an Appropriate Active-site Motif into a Hydrogen-evolution Catalyst with Thiomolybdate $[Mo3S13]^{2-}$ Clusters, *Nat. Chem.*, 2014, **6**, 248–253.

11 J. Mahmood, F. Li, S. Jung, M. S. Okyay, I. Ahmad, S. Kim, N. Park, H. Jeong and J. Baek, An Efficient and pH-universal Ruthenium-based Catalyst for the Hydrogen Evolution Reaction, *Nat. Nanotechnol.*, 2017, **12**, 441–446.

12 T. Reier, M. Oezaslan and P. Strasser, Electrocatalytic Oxygen Evolution Reaction (OER) on Ru, Ir, and Pt Catalysts: A Comparative Study of Nanoparticles and Bulk Materials, *ACS Catal.*, 2012, **2**, 1765–1772.

13 D. Wang, M. Gong, H. Chou, C. Pan, H. Chen, Y. Wu, M. Lin, M. Guan, J. Yang and C. Chen, Highly Active and Stable Hybrid Catalyst of Cobalt-Doped FeS2 Nanosheets-carbon Nanotubes for Hydrogen Evolution Reaction, *J. Am. Chem. Soc.*, 2015, **137**, 1587–1592.

14 H. Jin, H. Yu, H. Li, K. Davey, T. Song, U. Paik and S. Qiao, MXene Analogue: A 2D Nitridene Solid Solution for High-Rate Hydrogen Production, *Angew. Chem., Int. Ed.*, 2022, **61**, e202203850.

15 Z. Lu, Y. Li, X. Lei, J. Liu and X. Sun, Nanoarray Based "Superaerophobic" Surfaces for Gas Evolution Reaction Electrodes, *Mater. Horiz.*, 2015, **2**, 294–298.

16 J. Dukovic and C. W. Tobias, The Influence of Attached Bubbles on Potential Drop and Current Distribution at Gas-evolving Electrodes, *J. Electrochem. Soc.*, 1987, **134**, 331–343.

17 X. Zhao, H. Ren and L. Luo, Gas Bubbles in Electrochemical Gas Evolution Reactions, *Langmuir*, 2019, **35**, 5392–5408.

18 S. Oh, J. Han and J. Kim, Long-term Stability of Hydrogen Nanobubble Fuel, *Fuel*, 2015, **158**, 399–404.

19 Y. Sun, G. Xie, Y. Peng, W. Xia and J. Sha, Stability Theories of Nanobubbles at Solid–Liquid Interface: A Review, *Colloids Surf., A*, 2016, **495**, 176–186.

20 J. Qin, T. Xie, D. Zhou, L. Luo, Z. Zhang, Z. Shang, J. Li, L. Mohapatra, J. Yu, X. Hai and X. Sun, Kinetic Study of Electrochemically Produced Hydrogen Bubbles on Pt Electrodes with Tailored Geometries, *Nano Res.*, 2021, **7**, 2154–2159.

21 D. Lohse and X. Zhang, Surface Nanobubbles and Nanodroplets, *Rev. Mod. Phys.*, 2015, **87**, 981.

22 B. Tan, H. An and C. D. Ohl, Surface Nanobubbles are Stabilized by Hydrophobic Attraction, *Phys. Rev. Lett.*, 2018, **120**, 164502.

23 M. P. Brenner and D. Lohse, Dynamic Equilibrium Mechanism for Surface Nanobubble Stabilization, *Phys. Rev. Lett.*, 2008, **101**, 214505.

24 B. Tan, H. An and C. D. Ohl, Stability Dynamics and Tolerance to Undersaturation of Surface Nanobubbles, *Phys. Rev. Lett.*, 2019, **122**, 134502.

25 A. Angulo, P. van der Linde, H. Gardeniers, M. Modestino and D. F. Rivas, Influence of Bubbles on the Energy Conversion Efficiency of Electrochemical Reactors, *Joule*, 2020, **4**, 555–579.

26 Q. Chen, L. Luo, H. Faraji, S. W. Feldberg and H. S. White, Electrochemical Measurements of Single H_2 Nanobubble Nucleation and Stability at Pt Nanoelectrodes, *J. Phys. Chem. Lett.*, 2014, **5**, 3539–3544.

27 L. Luo and H. S. White, Electrogeneration of Single Nanobubbles at Sub-50-nm-radius Platinum Nanodisk Electrodes, *Langmuir*, 2013, **29**, 11169–11175.

28 Q. Chen, H. S. Wiedenroth, S. R. German and H. S. White, Electrochemical Nucleation of Stable N_2 Nanobubbles at Pt Nanoelectrodes, *J. Am. Chem. Soc.*, 2015, **137**, 12064–12069.

29 M. A. Edwards, H. S. White and H. Ren, Voltammetric Determination of the Stochastic Formation Rate and Geometry of Individual H_2, N_2, and O_2 Bubble Nuclei, *ACS Nano*, 2019, **13**, 6330–6340.

30 K. Kashiwagi, T. Hattori, Y. Samejima, N. Kobayashi and S. Nakabayashi, Hydrogen Nanobubbles at Roughness-Regulated Surfaces: Why Does the Standard Hydrogen Electrode Need a Platinized Platinum Electrode?, *J. Phys. Chem. C*, 2019, **123**, 7416–7424.

31 S. Lou, Z. Ouyang, Y. Zhang, X. Li, J. Hu, M. Li and F. Yang, Nanobubbles on Solid Surface Imaged by Atomic Force Microscopy, *J. Vac. Sci. Technol., B: Microelectron. Nanometer Struct.--Process., Meas., Phenom.*, 2000, **18**, 2573–2575.

32 X. Zhang, N. Maeda and V. S. Craig, Physical Properties of Nanobubbles on Hydrophobic Surfaces in Water and Aqueous Solutions, *Langmuir*, 2006, **22**, 5025–5035.

33 R. Hao, Y. Fan, M. D. Howard, J. C. Vaughan and B. Zhang, Imaging Nanobubble Nucleation and Hydrogen Spillover During Electrocatalytic Water Splitting, *Proc. Natl. Acad. Sci. U. S. A.*, 2018, **115**, 5878–5883.

34 S. Xu, X. Yu, Z. Chen, Y. Zeng, L. Guo, L. Li, F. Luo, J. Wang, B. Qiu and Z. Lin, Real-time Visualization of the Single-nanoparticle Electrocatalytic Hydrogen Generation Process and Activity under Dark Field Microscopy, *Anal. Chem.*, 2020, **92**, 9016–9023.

35 S. Wang, X. Shan, U. Patel, X. Huang, J. Lu, J. Li and N. Tao, Label-free Imaging, Detection, and Mass Measurement of Single Viruses by Surface Plasmon Resonance, *Proc. Natl. Acad. Sci. U. S. A.*, 2010, **107**, 16028–16032.

36 K. M. Bolles, F. Cheng, J. Burk-Rafel, M. Dubey and D. M. Ratner, Imaging Analysis of Carbohydrate-modified Surfaces Using ToF-SIMS and SPRi, *Materials*, 2010, **3**, 3948–3964.

37 S. Fang, H. Lee, A. W. Wark and R. M. Corn, Attomole Microarray Detection of MicroRNAs by Nanoparticle-amplified SPR Imaging Measurements of Surface Polyadenylation Reactions, *J. Am. Chem. Soc.*, 2006, **128**, 14044–14046.

38 J. Y. Kim, K. Lee, N. E. Coates, D. Moses, T. Nguyen, M. Dante and A. J. Heeger, Efficient Tandem Polymer Solar Cells Fabricated by All-solution Processing, *Science*, 2007, **317**, 222–225.

39 E. D. Gadea, Y. A. Perez Sirkin, V. Molinero and D. A. Scherlis, Electrochemically Generated Nanobubbles: Invariance of the Current with Respect to Electrode Size and Potential, *J. Phys. Chem. Lett.*, 2020, **11**, 6573–6579.

40 J. P. Bouanich and Site-site Lennard-Jones, Potential Parameters for N_2, O_2, H_2, CO and CO_2, *J. Quant. Spectrosc. Radiat. Transfer*, 1992, **47**, 243–250.

41 H. Berendsen, J. Grigera and T. Straatsma, The Missing Term in Effective Pair Potentials, *J. Phys. Chem.*, 1987, **91**, 6269–6271.

42 H. Heinz, R. A. Vaia, B. L. Farmer and R. R. Naik, Accurate Simulation of Surfaces and Interfaces of Face-centered Cubic Metals Using 12 − 6 and 9 − 6 Lennard-Jones Potentials, *J. Phys. Chem. C*, 2008, **112**, 17281–17290.

43 S. Plimpton, Fast Parallel Algorithms for Short-range Molecular Dynamics, *J. Comput. Phys.*, 1995, **117**, 1–19.

44 Y. A. Perez Sirkin, E. D. Gadea, D. A. Scherlis and V. Molinero, Mechanisms of Nucleation and Stationary States of Electrochemically Generated Nanobubbles, *J. Am. Chem. Soc.*, 2019, **141**, 10801–10811.

45 J. Newman and K. E. Thomas-Alyea, *Electrochemical Systems*, John Wiley & Sons, 2004.

46 J. A. Leistra and P. J. Sides, Voltage Components at Gas Evolving Electrodes, *J. Electrochem. Soc.*, 1987, **134**, 2442–2446.

47 H. Vogt and R. J. Balzer, The Bubble Coverage of Gas-evolving Electrodes in Stagnant Electrolytes, *Electrochim. Acta*, 2005, **50**, 2073–2079.

48 J. Eigeldinger and H. Vogt, The Bubble Coverage of Gas-evolving Electrodes in a Flowing Electrolyte, *Electrochim. Acta*, 2000, **45**, 4449–4456.

49 J. Newman, Scaling with Ohm's law; Wired vs. Wireless Photoelectrochemical Cells, *J. Electrochem. Soc.*, 2013, **160**, F309–F311.

50 A. J. Bard and L. R. Faulkner, *Electrochemical Methods: Fundamentals and Applications*, Wiley, New York, 2nd edn, 2001.

51 N. Pande, G. Mul, D. Lohse and B. Mei, Correlating the Short-time Current Response of a Hydrogen Evolving Nickel Electrode to Bubble Growth, *J. Electrochem. Soc.*, 2019, **166**, E280–E285.

52 L. Zhang, Y. Zhang, X. Zhang, Z. Li, G. Shen, M. Ye, C. Fan, H. Fang and J. Hu, Electrochemically Controlled Formation and Growth of Hydrogen Nanobubbles, *Langmuir*, 2006, **22**, 8109–8113.

53 X. Shan, I. Diez-Perez, L. Wang, P. Wiktor, Y. Gu, L. Zhang, W. Wang, J. Lu, S. Wang and Q. Gong, Imaging the Electrocatalytic Activity of Single Nanoparticles, *Nat. Nanotechnol.*, 2012, **7**, 668–672.

54 D. Jiang, Y. Jiang, Z. Li, T. Liu, X. Wo, Y. Fang, N. Tao, W. Wang and H. Chen, Optical Imaging of Phase Transition and Li-ion Diffusion Kinetics of Single LiCoO$_2$ Nanoparticles during Electrochemical Cycling, *J. Am. Chem. Soc.*, 2017, **139**, 186–192.

55 X. Shan, U. Patel, S. Wang, R. Iglesias and N. Tao, Imaging local electrochemical Current via Surface Plasmon Resonance, *Science*, 2010, **327**, 1363–1366.

56 J. Chen, K. Zhou, Y. Wang, J. Gao, T. Yuan, J. Pang, S. Tang, H. Chen and W. Wang, Measuring the Activation Energy Barrier for the Nucleation of Single Nanosized Vapor Bubbles, *Proc. Natl. Acad. Sci. U. S. A.*, 2019, **116**, 12678–12683.

57 K. Nakamoto, R. Kurita, O. Niwa, T. Fujii and M. Nishida, Development of a Mass-Producible On-chip Plasmonic Nanohole Array Biosensor, *Nanoscale*, 2011, **3**, 5067–5075.

58 P. Attard, Friction, Adhesion, and Deformation: Dynamic Measurements with the Atomic Force Microscope, *J. Adhes. Sci. Technol.*, 2002, **16**, 753–791.

59 S. Maheshwari, M. Van Der Hoef, J. Rodríguez Rodríguez and D. Lohse, Leakiness of Pinned Neighboring Surface Nanobubbles Induced by Strong Gas–Surface Interaction, *ACS Nano*, 2018, **12**, 2603–2609.

60 R. B. Schasfoort, *Handbook of Surface Plasmon Resonance*, Royal Society of Chemistry, 2017.

61 S. G. Lemay, Noise as Data: Nucleation of Electrochemically Generated Nanobubbles, *ACS Nano*, 2019, **13**, 6141–6144.

62 S. Maheshwari, M. van der Hoef, X. Zhang and D. Lohse, Stability of Surface Nanobubbles: A Molecular Dynamics Study, *Langmuir*, 2016, **32**, 11116–11122.

63 D. Dockar, M. K. Borg and J. M. Reese, Mechanical Stability of Surface Nanobubbles, *Langmuir*, 2018, **35**, 9325–9333.

64 F. Y. Ushikubo, T. Furukawa, R. Nakagawa, M. Enari, Y. Makino, Y. Kawagoe, T. Shiina and S. Oshita, Evidence of the Existence and the Stability of Nano-bubbles in Water, *Colloids Surf., A*, 2010, **361**, 31–37.

65 R. B. Anderson, James Bayer and L. J. E. Hofer, Linear Solutions of Fick's Law, *Ind. Eng. Chem. Process Des. Dev.*, 1965, **4**, 167–171.